This is a repository copy of *Multimodal single-molecule microscopy with continuously controlled spectral resolution*.

White Rose Research Online URL for this paper:
https://eprints.whiterose.ac.uk/177805/

Version: Published Version

eprints@whiterose.ac.uk
https://eprints.whiterose.ac.uk/

Multimodal single-molecule microscopy with continuously controlled spectral resolution

Jonathan Jeffet,[1,2,3] Ariel Ionescu,[4,5] Yael Michaeli,[1,2] Dmitry Torchinsky,[1,2,3] Eran Perlson,[4,5] Timothy D. Craggs,[6] and Yuval Ebenstein[1,2,3,*]

[1]Raymond and Beverly Sackler Faculty of Exact Sciences, Tel Aviv University, Tel Aviv, Israel; [2]Center for Nanoscience and Nanotechnology, Tel Aviv University, Tel Aviv, Israel; [3]Center for Light Matter Interaction, Tel Aviv University, Tel Aviv, Israel; [4]Department of Physiology and Pharmacology, Sackler Faculty of Medicine, Tel Aviv University, Tel Aviv, Israel and [5]Sagol School of Neuroscience, Tel Aviv University, Tel Aviv, Israel; and [6]Sheffield Institute for Nucleic Acids, Department of Chemistry, University of Sheffield, Sheffield, United Kingdom

ABSTRACT Color is a fundamental contrast mechanism in fluorescence microscopy, providing the basis for numerous imaging and spectroscopy techniques. Building on spectral imaging schemes that encode color into a fixed spatial intensity distribution, here, we introduce continuously controlled spectral-resolution (CoCoS) microscopy, which allows the spectral resolution of the system to be adjusted in real-time. By optimizing the spectral resolution for each experiment, we achieve maximal sensitivity and throughput, allowing for single-frame acquisition of multiple color channels with single-molecule sensitivity and 140-fold larger fields of view compared with previous super-resolution spectral imaging techniques. Here, we demonstrate the utility of CoCoS in three experimental formats, single-molecule spectroscopy, single-molecule Förster resonance energy transfer, and multicolor single-particle tracking in live neurons, using a range of samples and 12 distinct fluorescent markers. A simple add-on allows CoCoS to be integrated into existing fluorescence microscopes, rendering spectral imaging accessible to the wider scientific community.

WHY IT MATTERS In modern optical microscopy, color is used as a way to distinguish between different types of biological information. Recording multiple colors is commonly done by filtering each color separately and composing a multicolor image. Thus, multicolor imaging increases the overall acquisition time and introduces errors as each color is acquired at a different instance in time. Our method, continuously controlled spectral resolution (CoCoS), allows to transform with a simple add-on any standard fluorescence microscope into a simultaneous multicolor imaging system that can visualize all colors at the same time. Using a simple optical trick, CoCoS enables us to control the sensitivity of color detection with a click of a button, therefore allowing us to effortlessly optimize color imaging in a wide variety of applications.

INTRODUCTION

In recent years, single-molecule fluorescence microscopy has become a vital instrument in the toolbox of biological, physical, and chemical exploration (1–3). Biological processes in general, and within the cell in particular, involve a plethora of interactions between various biomolecules and compounds. To understand these processes at the molecular level, one must record their dynamics and be able to distinguish different entities located within close proximity, usually at scales smaller than the resolution limit of standard optical mi-

croscopy (∼250 nm). A distinct advantage of fluorescence microscopy is the ability to image and track dynamic processes with molecular specificity, allowing for the exploration of multimolecule functions and their building blocks. This specificity is achieved by tagging different molecular species with unique fluorescent reporters, enabling the discrimination of these molecules by the distinctive photophysical characteristics of the markers.

Multiplexing is most commonly achieved by differentiating the markers' spectral properties. Methods for spectral discrimination between different markers (4) fall roughly into three categories: 1) color channel separation by sequential switching of emission filters (5), 2) simultaneous multicolor imaging by color channel splitting of the imaged field of view (FOV) (6), and 3)

---

simultaneous localization and spectral imaging by insertion of a dispersive element in one light path of a split FOV (7−11). A table summarizing the pros and cons of existing configurations is presented in Table S1.

Although sequential channel imaging is simple to assemble and allows the largest FOV of up to $120 \times 120 \ \mu m^2$ (5), it comes at the cost of both linearly increasing acquisition time with each additional spectral channel and the loss of temporal synchronization between those channels. The latter limitation prohibits any multicolor registration of dynamic processes with timescales shorter than the filter switching such as in single-molecule Förster resonance energy transfer (smFRET) (12) measurements and multicolor tracking of many biological and physical processes. Multicolor splitting of the FOV overcomes synchronization limitations and maintains the simultaneous acquisition of discrete color channels but compromises throughput because of the reduced FOV that falls off reciprocally with the number of channels.

To address these problems, spectral imaging was introduced (13−16), followed by the implementation of its concepts to single-molecule super-resolution microscopy by multiple groups (7−10). Generally, spectral imaging is performed by the insertion of dispersive elements to the emission path, which converts the spectra into spatial intensity distributions. To calibrate the spectral distribution, a comparison to the nondispersed intensity profile is generally required. This is achieved either by prior knowledge of the spatial emitters pattern (15,16) or, more commonly, by simultaneously acquiring a diffraction-limited achromatic localization image (7,9,10,17,18). Spectral imaging enables to distinguish between markers presenting minute spectral differences (10,11,19−23); thus, in addition to characterizing markers by their spectra, it allows for the simultaneous mapping (8,18) or tracking (11,24) of spectrally similar markers using a single laser excitation.

Achieving efficient multicolor detection with spectral imaging requires setting the spectral resolution of the experimental system by a careful design of spectral properties of either the dispersive element (13,18,25) or sample (14). This is due to the underlying principle of spectral imaging, namely that higher spectral resolution is achieved by larger spectral dispersion, which in turn leads to poorer sensitivity and throughput. The sensitivity, measured by the signal/noise ratio (SNR), is reduced with the increase in spectral resolution (19,25) as the emitted photons are spread over more pixels, each contributing to the readout noise. Likewise, increased spectral resolution also results in loss of camera real estate, reducing the overall throughput by restricting the imaged FOV size (24) and the marker density to avoid spectral signal overlaps (19). As a result,

the FOV sizes of single-molecule spectral imaging schemes are small, ranging between 100 and 515 μm^2 (7,9,10,17,18,24), 30−144-fold smaller compared with sequential color channel imaging. The limit on marker density can be removed by applying super-resolution techniques in which only a sparse subset of markers is emitting in each frame of a multiframe acquisition (18,19,25−27). This, however, is achieved at the cost of significantly increased acquisition time per FOV because of the numerous frames required for reproducing the final image. Moreover, the spectral range of detected molecules still needs to be contained to small pixel areas to avoid overlaps in the sparse image and to maintain workable single-molecule sensitivity. Therefore, previous spectral super-resolution works were restricted to the spectral resolution of dyes within the same spectral window (usually far-red) excited with a single excitation laser (7,8,18,19,22,26), not exploiting the range of available dyes and limited to working with high spectral resolutions and lower throughputs.

The general consequence of the above discussion is that the optimal spectral resolution is achieved by the minimal dispersion that still allows to resolve the experimental question and, therefore, is experiment and sample dependent (18). For example, in an experiment needing to differentiate dyes with 10 nm spectral separation as presented in (8), a high spectral resolution is required (~1 nm/pixel), although this high resolution will be counterproductive in an experiment differentiating between dyes with 100 nm spectral separation as in (9) (resulting in an area of >500 pixel^2 per single-molecule spectra). Nonetheless, in current single-molecule spectral systems, there is no option for rigorous control over the spectral resolution other than replacing the dispersive element or manually adjusting its position in the optical setup (9,18,28). The lack of spectral resolution control forces setting the spectral resolution with the optical assembly and therefore drives the spectral imaging community to maximize the spectral resolution (19) instead of optimizing it per application or marker configuration, as is commonly done with nonspectral color imaging methods. This results in an incompetability of spectral imaging with various single-molecule applications involving markers spanning large spectral ranges such as in smFRET. Furthermore, because the dispersion in the spectral FOV is constant, spectral imaging methods need to register a localization image in a different channel. This is achieved either by dividing the emission photons between the spectral and localization channels (9,19,23,24), resulting in reduced localization and spectral accuracy (17,25), or by using a dual objective configuration (8,27,28), which results in complex optical setup and is limited to thin transparent samples. Both of these possibilities require

delicate alignment and registration of the localization and spectral channels, resulting in the limited distribution of spectral imaging, with just a handful of specialized labs using the method.

Here, we present continuously controlled spectral-resolution (CoCoS) microscopy for single-molecule spectral imaging, which allows continuous tuning of chromatic dispersion, thus giving full control over the spectral resolution of the system. Taking inspiration from an apparatus designed for atmospheric dispersion correctors in earth-bound telescopes (29), we positioned two identical direct vision prisms (also called double Amici prisms (30)) in the emission path of an epi-fluorescence microscope. These are used to introduce continuously controlled chromatic dispersion to the image for multicolor single-molecule detection and spectral analysis. A direct vision prism consists of three triangular prisms cemented together, with the two outer prisms identical to one another. The compound prism is built such that the light of a given wavelength passes straight through unperturbed (the incident and emergent rays remain parallel with no change to the optical axis), whereas the light of longer and shorter wavelengths is dispersed in opposite directions relative to this axis. When a pair of identical double Amici prisms are aligned on the optical axis, their dispersion will accumulate to give double the dispersion of a single prism. When these prisms are rotated about the optical axis in opposite directions by $\pm 90°$, their dispersion will completely cancel out, allowing for conventional super-resolution localization with minimal photon losses. Mounting the prisms on motorized rotators that can rotate the prisms independently about the optical axis enables us to continuously fine-tune the dispersion with a scaling law (31) of

$$D(\lambda) = 2\mathrm{D_{SP}}(\lambda) \cdot \sin\left(\frac{180° - RPA}{2}\right), \quad (1)$$

where D is the total dispersion at wavelength λ, $\mathrm{D_{SP}}$ is the single prism dispersion, and the relative prism angle (RPA) takes values between $0° \leq RPA \leq 180°$ (see Fig. 1 a for the illustration).

CoCoS offers the capability to tune and optimize the spectral resolution in real time to maximize both sensitivity and throughput. This presents both the flexibility to operate in different imaging modalities on a single microscope and the ability to switch between these modalities rapidly on the same sample. Furthermore, the CoCoS capability is easily added to existing single-molecule setups, in a simple modular upgrade, allowing it to be integrated with any fluorescence microscope without compromising its original function. Here, we establish the principle of CoCoS and then demonstrate three imaging modalities that correspond with key single-molecule

assays: spectral analysis, smFRET, and multicolor detection with single-particle tracking.

MATERIALS AND METHODS

Optical setup

Excitation

The excitation module was composed of five lasers (Cobolt, Solna, Sweden) with wavelengths spanning the visible to near-infrared spectrum: 405 nm (MLD 405, 250 mW max power), 488 nm (MLD 488, 200 mW max power), 561 nm (Jive 561, 500 mW max power), 638 nm (MLD 638, 140 mW max power), and 785 nm (NLD 785, 500 mW max power). All lasers were mounted on an in-house designed heat sink, which coarse aligned their beam heights. Each laser beam was passed through a clean-up filter (LL01-405-12.5, LL01-488-12.5, LL01-561-12.5, LL01-638-12.5, or LL01-785-12.5; Semrock, Rochester, NY) and expanded to 12.5−20× its original diameter (LB1945-A, 4× LB1157-A, 3× LB1437-A, LD2746-B, or LB1901-B; Thorlabs, Newton, NJ). Two motorized shutters (SH05; Thorlabs) were used for modulating on/off the solid-state 561 and 785 nm lasers because of long warm up times. The beams were then combined to a single beam using long-pass filters LP1−LP4, shown in Fig. 1 b (LP1: Di03-R405-t1-25.4D, LP2: Di03-R488-t1-25.4D, LP3: Di03-R561-t1-25.4D, and LP4: Di03-R635-t1-25.4D; Semrock). To homogenize the excitation profile of the sample, the combined beam was passed through an identical setup to the one described in the work of Douglass et al. (5). In short, the combined beam was injected into a compressing telescope (AC254-150-A-ML or AC254-050-A-ML; Thorlabs) with a rotating diffuser (24-00066; SUSS MicroOptics, Hauterive, Switzerland) placed ∼5 mm before the shared focal points of the telescope lenses (see Fig. 1). A series of six silver mirrors (PF10-03-P01; Thorlabs) was then used to align the beam into a modified microscope frame (IX81; Olympus, Tokyo,Japan) through two identical microlens arrays (2× MLA, 18-00201; SUSS MicroOptics) separated by a distance equal to the microlenses' focal length and placed inside the microscope frame. The homogenized beam was reflected onto the objective lens (UPlanXApo 60× NA1.42; Olympus) by a five-band multichroic mirror (MM, zt405/488/561/640/785rpc, Chroma Technology, Bellows Falls, VT or Di03-R405/488/532/635, Semrock in the axonal transport experiment). The sample was placed on top of a motorized XYZ stage (MS-2000; Applied Scientific Instrumentation, Eugene, OR) with 890-nm light emitting diode-based autofocus system (CRISP; Applied Scientific Instrumentation), which enabled scanning through multiple fields of view.

Emission

The emitted light from the fluorescent samples was gathered by the same objective and transmitted through the MM onto a standard Olympus tube lens to create an intermediate image at the exit of the microscope frame. This image was passed through a multinotch filter (MNF, NF03-405/488/561/635E combined with a 785-nm notch filter NF03-785E-25 in the silica beads experiments apart from the four-color bead shown in Fig. 2; FF01-440/521/607/694/809-25 multi-band filter combined with the same 785-nm notch filter in the smFRET experiment and the four-color bead shown in Fig. 2; and NF03-405E-25 single notch filter in the axonal transport experiment; Semrock) to block all residual laser light. Light was then directed into a magnifying telescope (Apo-Rodagon-N 50 mm and AC08-075-A-ML, Thorlabs or Apo-Rodagon-N 80 mm, Qioptiq, Göttingen, Germany in the smFRET and the four-color bead experiments), with two commercial direct vision prisms (117240; Equascience, Angerville, France) placed within the infinity space between the lenses

and mounted on two motorized rotators (8MR190-2-28; Altechna, Vilnius, Lithuania) controlling the prisms' angles around the optical axis. The final image was acquired on a back-illuminated scientific complementary metal-oxide-semiconductor camera (Prime BSI; Teledyne Photometrics, Tucson, AZ).

Image acquisition was coordinated using the Micro-Manager software (32), controlling camera acquisition, laser excitation, XY stage location, and prism rotator angles. The camera and lasers excitation were synchronized using in-house built TTL controller based on an Arduino Uno board (Arduino, Scarmagno, Italy) (33).

Sample preparation

Multicolor silica beads

For the labeling reaction, 5 μL of 1% suspension of azide-functionalized 100-nm silica beads in aqueous solution (Si100-AZ-1; Nanocs, New York, NY) were diluted in 20 μL doubly deionized H_2O (DDW) and sonicated for 1 h. Next, the beads were labeled using a copper-free click chemistry reaction with various dibenzocyclooctyl (DBCO)-activated fluorescent dyes, according to the experiment.

Five-color beads

A total of 0.53 mM DBCO-activated dyes (Alexa Fluor (AF) Dye 568-DBCO, Click Chemistry Tools, Scottsdale, AZ; IRDye 800CW-DBCO; LI-COR Biosciences, Lincoln, NE; and AF647-DBCO, AF488-DBCO, and AF405-DBCO, Jena Bioscience, Jena, Germany) were added to the beads solution with a relative ratio of 2:1:1:1:2, corresponding to AF405/AF488/AF568/AF647/IrDye 800CW. The beads and dye solution was vortexed and pipetted vigorously to homogenously distribute all dyes and left overnight at 37°C for the click reaction. Next, ethanol-isopropanol precipitation was used to remove excess dye molecules. Isopropanol cooled to −20°C was added to the beads and dye solution to a final volume of 1 mL. The solution was centrifuged at 4°C for 35 min at 18,000 rpm, creating a pellet of labeled beads at the bottom of the tube in a solution of excess dyes and isopropanol. The solution was carefully removed without disrupting the beads pellet. The same procedure was then repeated with cooling to −20°C 100% ethanol and then with cooling to −20°C 70%/30% ethanol/DDW solution. Finally, the labeled beads were suspended in 50 μL DDW to create a stock solution. For imaging the beads, 3 μL of the stock solution was added to 20 μL TE buffer (10 mM Tris and 1 mM EDTA (pH 8)) mixed with 4 μL of 2 mM DTT and placed on precleaned coverglass.

Far-red beads

For the far-red beads experiment, the same procedure was followed mixing a single 75 μM DBCO/BCN activated dye (AF647-DBCO and Cy5.5-DBCO; Jena Bioscience; CF640R-BCN, Biotium, Fremont, CA) with the azide-covered nanobeads to create three different stock solutions. Because of high background noise caused by unreacted dyes, which became prominent because of the high dispersion in this experiment, we added another cleaning step at the end of the previous ethanol-isopropanol precipitation with drop dialysis on 0.05-μm pore membranes (VMWP02500, MF-Millipore Membrane Filter, 0.05 μm pore size; Merck, Kenilworth, NJ).

smFRET

smFRET standards (12) of high, mid, and low FRET efficiencies (ATTO 550/ATTO 647N with 11-, 15-, and 23-bp (basepairs) separation between donor and acceptor, respectively) were each diluted to 0.5 nM in TE (pH 8) buffer and placed on silane-activated glass coverslips prepared according to an established protocol (34).

Animal models

Dorsal root ganglion (DRG) explants for axonal transport measurements were obtained from E12.5 mouse embryos of total three pregnant HB9::GFP mice. HB9::GFP (B6.Cg-Tg(Hlxb9-GFP)1Tmj/J) mice were originally obtained from The Jackson Laboratory (Bar Harbor, ME). The mouse colony was maintained by breeding with ICR mice. All animal experimentations were approved by the Animal Ethics Committee of Tel Aviv University.

Axonal transport of Qdot-labeled neurotrophins

Axonal transport of Qdot-labeled pro-brain-derived neurotrophic factor (BDNF), BDNF, and nerve growth factor (NGF) was tracked in axons of DRG neurons within microfluidic chambers.

Polydimethylsiloxane microfluidic chambers were prepared for DRG plating as previously described (35). Microfluidic chambers were adhered to Fluorodish 170 μm-thick glass-bottom plates (PD50-100; World Precision Instruments, Sarasota, FL) at 70°C for 20 min, followed by 10-min ultraviolet irradiation. The glass bottom within the microfluidic chambers was coated for 2 h at 37°C with Matrigel matrix (356234; Corning, Corning, NY) diluted 1:100 with 1× Dulbecco's phosphate-buffered saline. Meanwhile, DRG explants were isolated from E12.5 mouse embryos and maintained in 1× Hank's Buffered Saline Solution (14185-045; Gibco, Waltham, MA) until plating. After coating, Matrigel solution was removed, and three DRG explants were plated into the proximal channel of each microfluidic chamber. DRG explants were grown for the first 24 h with spinal cord explant Neurobasal medium (SCEx) containing Neurobasal (21103-049; Gibco), 2% B27 supplement (17504-044; Gibco), 1% Glutamax (35005-038; Gibco), 1% penicillin-streptomycin (03-031-1B; Biological Industries, Beit HaEmek, Israel), and 125 ng/mL mouse NGF (N-100; Alomone Labs, Jerusalem, Israel). 1 day after plating growth medium was refreshed and to improve the growth of axons into the distal compartment, an NGF gradient of 125 and 37.5 ng/mL was applied between the distal and proximal compartments, respectively. Once axons have extensively crossed into the distal compartment, the medium in both compartments was replaced with NGF- and B-27-depleted poor SCEx for 2-h neurotrophic starvation. Meanwhile, human BDNF-biotin (B-250-B; Alomone Labs), human pro-BDNF-biotin (B-256-B; Alomone Labs), and mouse NGF-biotin (N-240-B; Alomone Labs) were mixed separately in a molar ratio of 3:1 with Qdot-625 streptavidin, Qdot-565 streptavidin, and Qdot-800 streptavidin, respectively (Q10131MP; Q10143MP; and Q10173MP; Molecular Probes, Eugene, OR). Qdot-neurotrophin binding reaction was performed on ice for 30 min. After the 2-h starvation, all three Qdot-neurotrophins were added exclusively to axons in the distal compartment of microfluidic chambers for 40 min, followed by three consecutive washes with SCEx medium.

The final concentration of each neurotrophin introduced to axons was 100 ng/mL. To preserve pH and enable tracking of axonal transport in room temperature in the absence of 5% CO_2, medium in microfluidic chambers was replaced with HEPES-based Tyrodes' solution containing $CaCl_2$ (2 mM), KCl (2.5 mM), NaCl (119 mM), $MgCl_2$ (2 mM), glucose (20 mM), and HEPES (25 mM) (pH 7.4).

Acquisition parameters

All samples were imaged with the same hardware as described in the Optical setup of the Materials and methods. Because of various sample background and SNR conditions, sample-specific acquisition parameters were used and are reported herein.

Five-color beads

The image presented in Fig. 1 was acquired using sequential five-laser excitation (excitation order: 785, 638, 561, 488, and 405 nm)

with a single laser per camera frame. The laser intensities at the laser outputs were 400 mW for the 785 nm laser and 100 mW for all other lasers, 300 ms camera exposure per frame, and RPA = 174°.

For spectral calibration, 13 images with RPA ranging from 180 to 140° were imaged by sequential excitation of all five lasers. Laser intensities of 50 mW were used for all lasers, and 300 ms camera exposure was used per image (see Fig. S1).

Four-color bead

The image presented in Fig. 2 *b* was acquired using sequential four-laser excitation and a four-laser simultaneous acquisition, which was not presented in Fig. 2 *b* but is provided in the Supporting materials and methods (excitation order: 785, 638, 561, 488 nm, and all lasers simultaneously). The laser intensities at the laser outputs were 300, 50, 30, and 50 mW for the 785, 638, 561, and 488 nm lasers, respectively, with 100-ms camera exposure per frame and 10 prisms position according to the presented RPAs in the figure.

Far-red beads

All far-red bead samples (Fig. 3; Fig. S5) were imaged with the same acquisition parameters: the 638 nm laser at 30 mW at its output, 300 ms camera frame exposure and two frames per FOV, and no dispersion at 180° RPA and optimal dispersion at 120° RPA. The perpendicular shift between the two frames (along the *y* axis as presented in Fig. 3) is due to optical aberrations of the lenses L3 and L4, together with slight misalignment of the two prisms relative to the lenses' optical axis. At maximal dispersion values, the limited clear aperture of the prisms caused additional aberrations because of higher beam divergence, causing the light to deflect from the prisms' edges.

smFRET

For each FOV of a single smFRET species, a time lapse of alternating 638 and 561 nm laser excitations at 100 mW were taken, with 300-ms exposure per frame.

Axonal transport of Qdot-labeled neurotrophins

To detect the emission spectra of the three Qdots, a different set of filters and MM was used in this experiment (see Optical setup in Materials and methods). With this filter set, the pro-BDNF-Qdot 565 and BDNF-Qdot 625 proteins were imaged within the same spectral window, setting the limit of minimal dispersion to RPA = 174° for four pixels distance between the dispersed point spread functions (PSFs) of the two Qdots. The optimal experimental RPA was set to 172° to produce larger spectral separation between these Qdots and therefore enable spectral resolution in cases of motion-induced PSF smearing or out-of-focus PSF imaging. For each FOV, a time lapse of 80 acquisitions was taken. Each acquisition was composed of four consecutive dispersed images with RPA = 172° and 100-ms exposure time in the following order: without emission filter, 575/15 emission filter, 605/15 emission filter, and 809/81 emission filter. This was followed by a 400-ms pause and then the same four image acquisition with no dispersion (RPA = 180°) followed by another 400-ms pause. In all acquisitions, the sample was excited by 405 nm laser at 10 mW out of the laser head.

Data analysis

Spectral calibration

To enable a readout of the emission's wavelength, a calibration between the intensity shifts in the image and the spectral information encoded within is needed. These shifts in the image domain result

from the basic prisms' dispersion curve ($D_{SP}(\lambda)$ in Eq. 1) and the RPA value as described in Eq. 1. To measure $D_{SP}(\lambda)$ of the prisms (because the materials of the prisms were unknown to the supplier, and therefore, a theoretical dispersion curve could not be calculated), images of the same five-color bead excited sequentially with five-laser excitations at 13 different RPAs were analyzed. For each RPA, the bead's intensity maxima per excitation source were localized, and the *y* distance from the peak of the achromatic image with RPA = 180° was calculated. To reduce localization errors because of the high FRET experienced with this sample, we subtracted from each image the rescaled images of higher wavelength excitations taken with the same RPA (for example, for localizing the orange peak excited by the 561 nm laser, the images of 638 and 785 nm excitations were rescaled to the orange emission image and subtracted from it). Each spectral window *y* distances were then plotted and linearly fitted against sine of (180 − RPA)/2 to extract the maximal dispersion values corresponding to 2 $D_{SP}(\lambda)$ at the maximal emission wavelengths (see Fig. S1). Next, to better characterize the $D_{SP}(\lambda)$ along the entire spectrum, we wanted to use more than five wavelength measurements; therefore, we summed images with different excitation at the same RPA and localized the minima between emission peaks in images of RPA $\geq$ 166° were these minima resolvable. These minima correspond with the filter's laser line notches, giving us an additional four measurement points for the dispersion calibration curve (see Fig. S2). The same linear fit to the *y* distances of minima values was performed to extract the maximal dispersion per notch wavelength (Fig. S1). Next, the fitted maximal dispersion values, plotted against the wavelengths of fluorophores emission peaks and the wavelengths of filter notches, were fitted to a third order polynomial using MATLAB (The MathWorks, Natick, MA) curve fitting tool ("least absolute residuals" robust fitting method), as presented in Fig. S3. The output of this fit is a calibration curve between maximal dispersion values of the CoCoS system in pixel units and the emission wavelength. With this calibration, we can transform intensity shifts in the image to spectral registration of the emission in wavelength units. Moreover, with the inverse transformation, from wavelength to pixel displacement, it is also possible to calculate the theoretical RPA values for the optimal dispersion needed to spectrally resolve emitters.

Optimal RPA calculation

The optimal RPA values presented in Table 1 were calculated according to Eq. 1 using the wavelength to pixel calibration obtained in the previous section and the dyes' maximal emission wavelength values obtained from their vendors' websites. For dyes with emission maxima at different emission channels, the minimal spectral resolution was defined as four pixels separation between dispersed maxima. This separation would allow for dispersion of the spectra enough to achieve separation larger than the dyes PSFs (~3 pixels in diameter, according to Rayleigh criterion), allowing us to clearly distinguish between them and removing the need for full spectral characterization. Because color channel separation only requires small dispersion values, the PSFs themselves do not stretch considerably and only displace in position (see Table S2 showing that the stretching of PSF because of dispersion is usually smaller than the PSF itself), confirming that four pixels suffice for spectral separation.

The minimal dispersion needed to spectrally resolve a pair of dyes within the same spectral window was defined as three-pixel separation. In this case, we separate the dyes by spectral analysis, which allows for resolution of spectral maxima varying with only three pixels resolution (as was shown with CF640R and AF647 in Fig. 3). For dyes with emission maxima outside of the emission channels transmission, the channel's closest edge to the maxima was used as the emission's maximum for calculating the minimal dispersion.

Far-red beads spectra extraction

Spectra extraction and analysis were performed by in-house written scripts in MATLAB. First, to calculate the average spectra of the red dyes-labeled beads, samples of single bead type were analyzed in the following manner. Initially, peak calling using the "FastPeak-Find" function (36) was performed on the localization (180° RPA) images of multiple FOV (∼8−20 depending on bead concentrations) per bead sample. Beads separated by distances shorter than the dispersion at the optimal RPA of 120° (<70 × 6 pixels^2) were discarded. Next, for each bead location, we searched for local maxima in the dispersed image (RPA 120°) to find for any location shifts perpendicular to the dispersion axis due to aberrations (both by the telescope lenses L3 and L4 and because of the limited clear aperture of the prisms causing aberrations in large dispersion values). Next, intensity profiles were extracted from the dispersed images by taking the mean intensity values of 70 × 6 pixels^2 crops around the corrected bead locations and Gaussian filtered with 1 pixel sigma (filtering was performed to reduce the effect of the Poisson distributed noise (25) more evident in the dispersed image because of the lower SNR). Bead profiles in which the SD of the intensity profile was lower than twice the SD of the background around the profile were discarded because of low SNR that would compromise the spectral analysis. The remaining intensity profiles' x-values were taken to be the displacement values from the bead location in the dispersion axis (i.e., x = 0 is the location of the bead in the nondispersed image). All profiles were then normalized between 0 and 1 and adjusted from pixel displacement values to wavelength, according to the spectral calibration curve. To produce the average spectrum of a single dye used for the bead classification process, all normalized profiles originating from the same red dye beads were averaged (see Figs. S6 and S7).

Optical distortion of the FOV induced by the L3 and L4 telescope lenses had created spectral shifts corresponding to beads locations in the FOV. These shifts were corrected by registering the spectral shifts compared with the median spectrum of multiple single dye bead samples (see Fig. S11) and fitting these shifts as a function of the beads spatial location to create a calibration matrix. The fitting was performed using MATLAB's surface fit tool with local quadratic regression model ("loess") and least absolute residuals robust fit (see Fig. S12). The fitted surface was later used to correct for optical aberration-induced spectral shifts both in the average spectra calculation and in the dye classification procedures.

Multi-far-red dyes classification

To analyze spectra from FOV containing a mixture of beads labeled with different red dyes, we first performed background subtraction because of high free dyes concentration. Median pixels values taken from multi-FOV stack were used as a background mask that was subtracted from the analyzed FOV using FIJI's (37) "calculator plus" plugin. Next, beads spectra were extracted from the background-subtracted FOV according to the procedure explained above. Spectra classification was done by cross correlating the extracted bead spectra with the average dye-specific reference spectrum obtained from FOVs containing single dye beads. The spectra were classified according to the highest cross correlation score between the three optional spectra, with all maximal correlation scores being above 0.9, indicating good agreement. In general, classification to Cy5.5 was relatively easy, with cross correlation scores varying substantially (mean difference from the next best score was 0.35), whereas classification between the CF640R and AF647 is harder (mean difference from the next best score was 0.040) for obvious reasons as the spectra are less distinguishable. The spectral classification process can be also done with the theoretical spectra with similar classification results (mean difference from the next best

score for Cy5.5 was 0.46 and CF640R and AF647 was 0.047), with lower overall scores, however, probably because of pixel/wavelength calibration inaccuracies (see Fig. S9).

smFRET

The analysis of the smFRET time lapses was carried out by the iSMS v2.01 software (38) based on MATLAB (version R2019b) and an additional custom MATLAB code. The analysis was performed following the standard procedure in the software's manual. The main difference is that the two regions of interest selected for the dual-channel analysis were overlapped on the entire FOV, which results in three to seven times larger FRET regions of interest compared with standard dual-color FRET total internal reflection fluorescence (TIRF) experiments. The FRET correction factors used in the analysis were calculated according to the procedure described in the recent work by Hellenkamp et al. (12) and were the following: direct excitation = 0.058 ± 0.068, donor leakage = 0.127 ± 0.048, γ-factor = 0.5541 ± 0.078, and β-factor = 1.77 ± 0.025. An elaborated account on the calculation of the various correction factors in this analysis is given in the Supporting materials and methods and in Figs. S14−S18. To assure that only single FRET pairs were analyzed per molecule, only time traces that presented a clear single bleaching step of either the acceptor or donor were taken into account in the analysis. Data points from the corrected FRET efficiency (E) and stoichiometry (S) time traces of each of the three different FRET samples (high/mid/low FRET) were plotted separately on two-dimensional (2d) histograms (see Fig. S16) and fitted by a Gaussian mixture model of two 2d Gaussians to disentangle the Gaussian measurement noise (random blinking/fluctuations of the fluorophore intensities) from the actual Gaussian distribution originating from the real E and S values. The more significant 2d Gaussian distribution out of the two was used to calculate the mean FRET efficiency value ⟨E⟩ for each sample (shown at the bottom of Fig. 5 *d*). These values were then used to calculate the FRET-averaged distance R$_{⟨E⟩}$, according to the following equation:

$$R_{\langle E \rangle} = R_0 \left(\langle E \rangle^{-1} - 1 \right)^{\frac{1}{6}}, \tag{2}$$

where R$_0$ is the Förster radius taken from (12). The FRET-averaged distance error was calculated according to the error propagation described by (12), taking into account the standard errors of ⟨E⟩ per sample, calculated from the Gaussian fits, and ΔR$_0$ taken to be 7% of R$_0$.

Axonal transport of Qdot-labeled neurotrophins

The optimal RPA was calculated by the same procedure explained previously with spectral windows corresponding to the filter set used in this experiment. All image analyses in this experiment were performed in Fiji (37), including the time averaging and background subtraction used to create Fig. 5 *b* and the generation of kymographs presented in Fig. 5 *e* by the Multi Kymograph plugin.

Data and materials availability

The authors declare that the main data supporting the findings of this study are available within the article and its Supporting materials and methods. Extra data are available from the corresponding author upon reasonable request. Raw videos and images used in this manuscript are available from the corresponding author upon reasonable request. All custom codes that were used to produce the images and data analysis in this study are available from the corresponding author upon reasonable request.
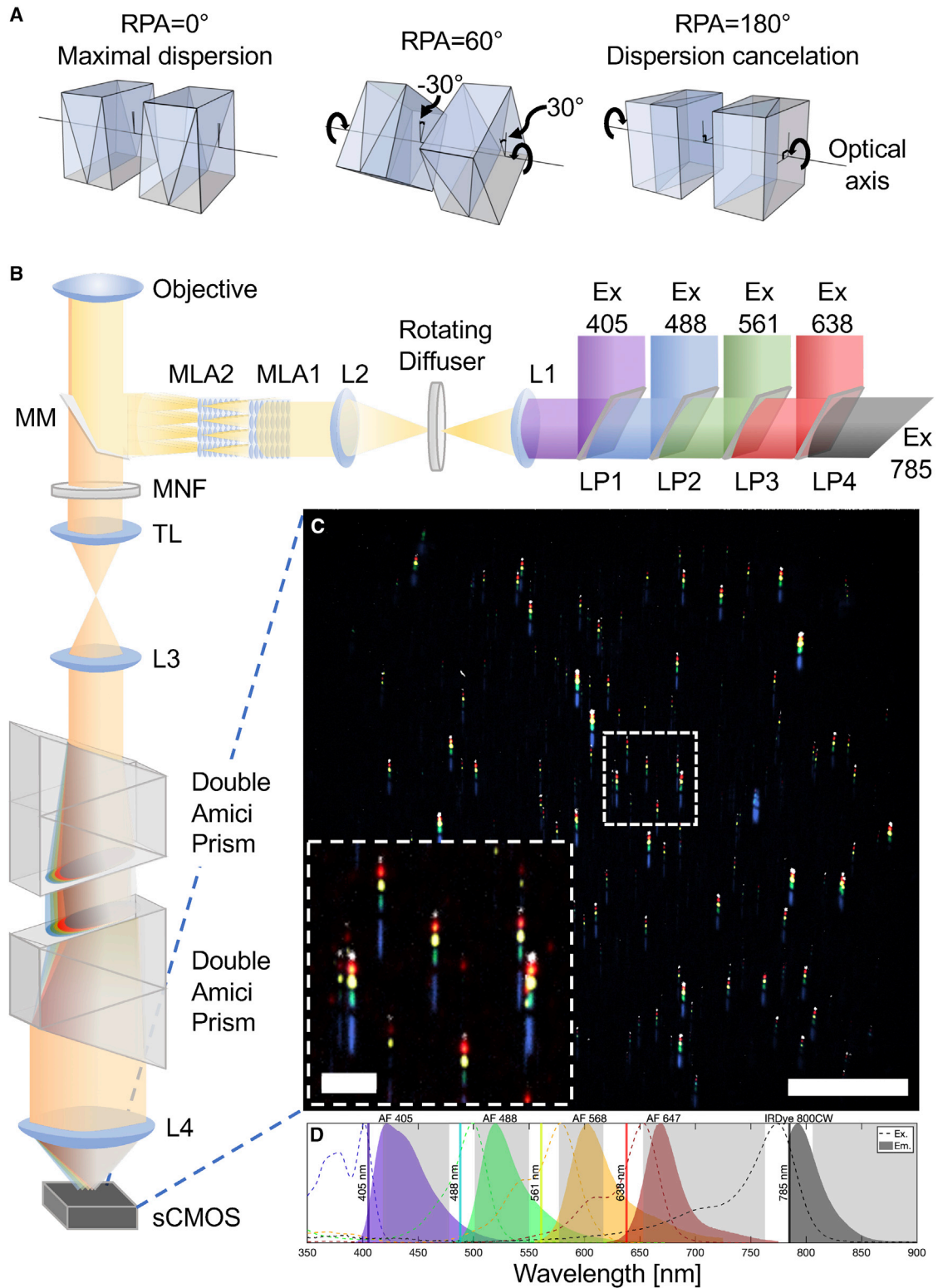
FIGURE 1 CoCoS microscopy. (*A*) Illustration of the prisms' rotation about the optical axis to control the total dispersion and its axis. The relative prisms angle (RPA) about the optical axis determines the total dispersion according to Eq. 1, whereas the global angle of both prisms at RPA = 0° sets the dispersion axis. (*B*) Optical scheme. Five excitation lasers (excitation 405, 488, 561, 638, and 785) are combined to a single beam and reshaped to give a uniform epi-illumination profile of 130 × 130 μm² in the sample plane. A MM with five spectral emission windows followed by an MNF set the emission channels of the system. The emission image is collimated out of the microscope's tube lens (TL) by a third lens (L3) and passed through two double Amici prisms located on motorized rotators. These rotating prisms allow the control of the total

(legend continued on next page)

RESULTS

Principle of CoCoS operation

The operational principle of the system is illustrated in Fig. 1 b with all technical details provided in the Materials and methods. Based on an inverted epi-fluorescence excitation scheme, we incorporated five lasers that fit the spectral windows of a five-band MM and the matching MNF. To increase acquisition throughput, the combined Gaussian laser beam was reshaped to flat-top illumination (5), providing a uniform excitation field of up to $130 \times 130 \ \mu m^2$. The emission signal was passed through two commercial low-cost double Amici prisms positioned on motorized rotators. The dispersion of the system is controlled by the rotators angle about the optical axis, permitting full computerized control over both the angle of the dispersion axis (global rotation of the two prisms) and the spectral resolution of the emission signal (controlled by the RPA). The full spectral resolution range presented in this work was scanned within 0.625 s with the rotators installed in our CoCoS system (rotation velocity of 48°/s). However, this depends solely on the rotation speed of the rotators and can be reduced to 10 ms with commercially available rotators (rotation velocity of >3000°/s). The double Amici prisms design, unlike other dispersive designs, maintains the optical axis of the system, eliminating the need for additional mirrors and significantly reduces the alignment complexity of the optical setup. Thus, the CoCoS module consisting of two rotatable prisms and a telescope (L3 and L4 in Fig. 1 b) can be used as an add-on to any existing fluorescence imaging microscopy scheme, with no need for additional alignment.

Continuous control of spectral resolution

We prepared a multicolor point source sample to validate the continuous dispersion control and calibrate the spectral resolution of the system. Azide-functionalized, 100-nm silica beads were stained with five DBCO-conjugated fluorescent dyes (Alexa Fluor 405, Alexa Fluor 488, Alexa Fluor 568, Alexa Fluor 647, and IrDye800CW) via copper-free click chemistry. The straightforward staining of the beads (any DBCO- or BCN-conjugated dye could be connected to the beads very efficiently) allowed for flexibility in dye selection and customization of the calibration

beads to our system. Fig. 1 c shows a representative FOV of five-color beads with the RPA set to 174°. With this RPA, all five-color windows of the beads (spectra presented in Fig. 1 d) are just resolvable, allowing differentiation between the colors while maintaining the highest SNR. As can be seen from the elongation of the blue channel in the figure, the fundamental dispersion of the prisms is nonlinear with respect to the wavelength, with higher dispersion at lower wavelengths reaching a plateau in the near infrared (see Figs. S1–S3).

The continuous control over the spectral resolution allows effortless toggling between three acquisition modalities during an experiment: 1) Localization mode with RPA = 180°; 2) color-detection mode, in which the different spectral channels are dispersed by the minimal resolvable amount; and 3) full spectral mode in which the detailed emission spectra of the fluorescent dyes can be determined with sub-nm wavelength resolution. The rapid alternation between modalities allows switching with a click of a button between experimental modes that previously would have required different optical setups altogether. This has many advantages, for example, in multicolor tracking (39) or time-resolved single-molecule spectroscopy (40,41), in which both localization precision and spectral information are important. With CoCoS, the localization or color detection could be made first with a single frame, immediately followed by continuous spectral or spatial recording, enabling the detection of environment-dependent spectral shifts or multiplex spatial dynamics.

We demonstrated the continuous control over the spectral resolution by imaging the same single silica bead labeled with four dyes (Alexa Fluor 488, Alexa Fluor 568, Alexa Fluor 647, and IrDye800CW) at various RPAs (Fig. 2). The optimal spectral resolution for color detection in these beads was achieved with an RPA = 174°, with the dyes just resolvable (Fig. 2, dotted red rectangle). Lower spectral resolution (higher RPA) does not allow differentiation between the dyes, whereas higher spectral resolution (lower RPA) results in the loss of throughput because of increased spreading of the molecule's image and decrease in SNR as the signal is spread over more pixels. Using Eq. 1, we calculated the optimal RPA for different commonly used dye pairs (Table 1), allowing four pixels between different color channels to avoid PSF overlap. As expected, dyes with more similar emission spectra require greater dispersion

dispersion of the CoCoS system by setting the RPA about the optical axis. The output beam is then focused onto a scientific complementary metal-oxide-semiconductor camera (sCMOS) camera by an imaging lens L4. (C) Representative false-color FOV of 100-nm silica beads labeled with five different fluorescent dyes (Alexa Fluor (AF) 405, 488, 568, and 647 and IRDye 800CW) and imaged with RPA set to 174°. Scale bars, 30 μm, inset 5 μm. (D) Excitation (dotted lines) and emission (solid color) spectra of the five-dye beads, plotted against the total emission spectral channels (gray rectangles, product of MM and MNF transmission values) of the CoCoS system. LP1-4, long-pass dichroic; MLA1-2, micro-lens array.
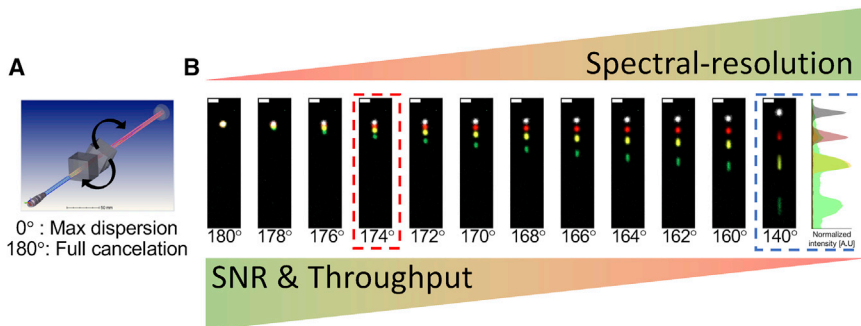
FIGURE 2 Spectral resolution control with CoCoS. (*A*) Illustration of the prism rotation about the optical axis. (*B*) Multiple false-color images of the same four-color bead consecutively excited with four excitation sources (Ex. 488, 561, 638, and 785) at different RPAs (depicted below each image). The spectral resolution is controlled by real-time motorized rotation of the two prisms, and the entire set of images was taken in under 2 s. The spectral resolution comes at the cost of spreading the emission photons on a larger pixel area. Thus, increased spectral resolution reduces the SNR and limits the maximal density of imaged molecules because of PSF overlaps. CoCoS allows for choosing the optimal spectral resolution according to the experimental need, toggling between three acquisition modalities: achromatic localization mode with full dispersion cancellation (180°), color-detection mode with optimal spectral resolution optimizing both throughput and SNR (for this dye combination achieved with RPA set to 174°, *red dotted rectangle*), and spectroscopy mode in which the full spectral information within the different emission channel windows is available at the expense of lower SNR (shown at RPA of 140° for presentation purposes, *blue dotted rectangle*). The spectra on the far right depicts an overlay of the average intensity line plot along the *y* axis after each excitation. All images are presented with the same brightness and contrast values showing the reduction in SNR as the dispersion increases. Scale bars, 1 μm.

(lower RPA) to resolve; compare, for example, Cy3-ATTO 550 (RPA = 152.2°) with Cy3-AF647 (RPA = 176.2°). When performing color detection on a multidye system, the lowest RPA between any dye pair in the experiment should be used.

In the case of the four-color beads, the spectral signature of the green and orange emission is already distinct at RPA = 140°, allowing us to characterize the AF488 and AF568 emission spectra (Fig. 2 *b*, *blue dotted rectangle*). The green spectral intensity profile (488-nm excitation) indicates high FRET from AF488 to AF568, shown by the high intensity distribution in both emission channels.

Resolving the shades of far-red fluorophores

Operating CoCoS in spectral mode by setting the dispersion to higher spectral resolutions enables us to distinguish between different dyes with emission spectra falling within the same emission band. Single-band multiplexing enables detecting spectrally close fluorophores with a single excitation laser and reduced chromatic aberrations. Moreover, applying single-band multiplexing to a multichannel scheme significantly increases the number of distinct observables in a single experiment, dramatically expanding the available color palette for biological experiments. We use CoCoS to extract the full spectral information and to distinguish between different markers in our far-red spectral band. Azide-functionalized, 100-nm silica beads were labeled with different red dyes (CF640R, AF647, and cyanine (Cy) 5.5) varying only slightly in their emission spectra (see Fig. S4). We set an RPA of 120° according to Eq. 1 and Table 1 to maintain a two- to three-pixel difference between the spectral maxima of the three dyes. A spectral image (RPA = 120°) was acquired together with a localization image (RPA = 180°) to determine the exact shift caused by the spectral dispersion (see Fig. 3, *b and c*; Fig. S5; Materials and methods). Spectra from the different beads

TABLE 1 Optimal RPA values for spectral distinction of selected dye pairs

	AF405	AF488	Cy 3	ATTO 550	AF555	AF568	AF594	CF 640R	AF647	Cy 5.5	IrDye 800CW
AF 405		178.3	178.7	178.7	178.7	178.8	178.9	179.0	179.0	179.1	179.2
AF 488	178.3		174.1	174.9	175.2	176.4	176.9	177.6	177.7	177.9	178.3
cy 3	178.7	174.1		152.2	161.4	173.2	175.0	176.0	176.2	176.8	177.7
ATTO 550	178.7	174.9	152.2		120.5	171.0	173.8	175.6	175.8	176.5	177.5
AF 555	178.7	175.2	161.4	120.5		169.3	173.1	175.3	175.5	176.3	177.4
AF 568	178.8	176.4	173.2	171.0	169.3		160.4	172.9	173.5	175.1	176.9
AF 594	178.9	176.9	175.0	173.8	173.1	160.4		170.3	171.3	173.9	176.5
CF 640	179.0	177.6	176.0	175.6	175.3	172.9	170.3		112.0	167.6	174.4
AF 647	179.0	177.7	176.2	175.8	175.5	173.5	171.3	112.0		164.6	174.0
cy 5.5	179.1	177.9	176.8	176.5	176.3	175.1	173.9	167.6	164.6		171.5
IrDye 800CW	179.2	178.3	177.7	177.5	177.4	176.9	176.5	174.4	174.0	171.5	

The presented RPA values were calculated for three or four pixels separation between emission maxima values of the dye pairs, for dyes in the same or different spectral channels, respectively. These separation values allow differentiation between the dyes while taking into account convolution with the emitters' PSF (~3 pixels in diameter for our system). See Materials and methods and Supporting materials and methods for additional information regarding the calculation procedure.
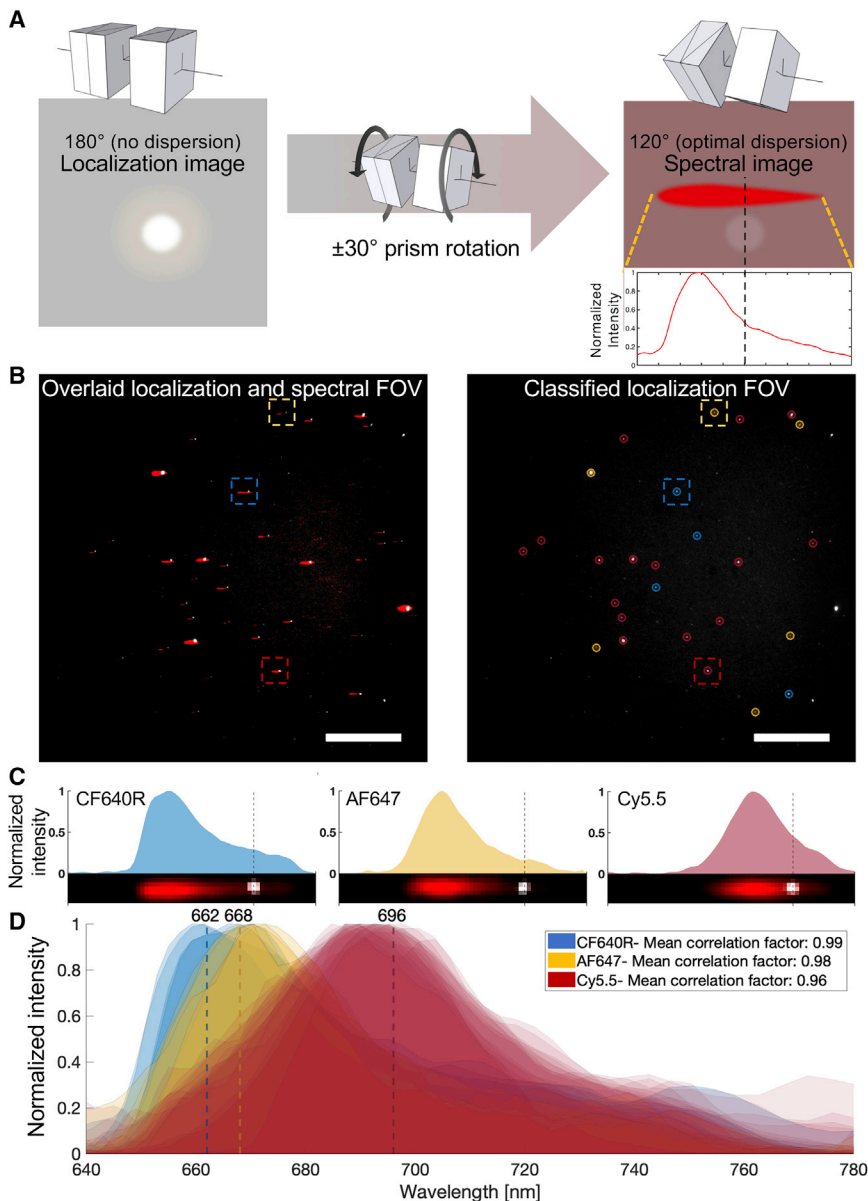
FIGURE 3 Resolving the shades of red dyes. (*A*) Schematic illustration explaining the procedure to obtain spectral information with CoCoS imaging. First, a localization image is captured using RPA of 180°, then the prisms are rotated to the optimal RPA for the spectral resolution of the imaged dyes (here 120°), and a second image is captured. An intensity profile of a molecule in the spectral image, with respect to the molecule's coordinates in the localization image, contains the emission spectrum of the molecule. (*B*) Three different red fluorophores were used to label 100-nm silica beads. The beads were mixed and imaged according to the procedure illustrated in (*A*), shown in the false-colored FOV image on the left. The localization image presented in white is overlaid on the spectral image in red, showing the dispersed molecular spectra. On the right, the localization image is shown after classification of the dyes according to their spectra using cross correlation of the individual spectrum with average dye spectra (see Materials and methods). Blue, yellow, and red refer to CF640R, AF647, and Cy 5.5, respectively. Colored dashed squares mark the molecules presented in (*C*). Scale bars, 30 μm. (*C*) Normalized spectral intensity profile of three selected molecules in (*B*). Cropped images of the molecules after alignment and Gaussian filtering of the spectral image is shown at the bottom. Dashed lines indicate the localization coordinate. (*D*) An overlay of all individual spectral profiles extracted from the FOV. Mean cross correlation scores used for the classification of the spectra are shown in the legend. Vertical lines show the theoretical emission maxima of the corresponding dyes' spectra, showing that molecular spectra with maxima differing by only ~6 nm are resolvable with CoCoS.

were then classified (as shown in Fig. 3) to the various dyes using cross correlation comparison with reference spectra obtained from single dye experiments (see Figs. S6 and S7) or by comparison with theoretical spectra (Figs. S8 and S9).

Using this procedure, we were able to differentiate, within the same FOV, between the three dyes and classify each bead according to its spectrum (see Fig. 3, *b and d*), showing that emission spectra with maxima differing by only 6 nm, as in the case of CF640R and AF647, are resolvable with the CoCoS system. Although two consecutive frames are required to provide the reference localization to calibrate the spectra, the cost in total acquisition time is negligible considering the fast switching and potential increased multi-

plexing (for example, there are six commercially available, well-separated dyes suitable for our red channel alone, see Fig. S10).

High-throughput epi-fluorescence smFRET quantification

Visualizing dynamic processes with multiple colors usually results in compromised accuracy because of the time delay between sequential acquisitions in the different channels. Spectral splitting of the FOV into two to four spectral channels bypasses this synchronization problem but results in more complex optics and data analysis, accompanied by significant loss of camera real estate with every additional channel. The CoCoS

system enables the simultaneous recording of multiple emission channels with single-molecule sensitivity while maintaining an extremely large FOV (130 × 130 μm^2). This configuration may be ideal for high-throughput smFRET experiments on surface-immobilized molecules. Such experiments are usually performed using TIRF illumination combined with FOV splitting, which results in a limited region for quantitative data acquisition. Here, we show that our CoCoS approach allows us to perform smFRET experiments on DNA molecules under epi-illumination, removing the need for complicated TIRF optics and postprocessing image registration while gaining significant increases in throughput from our large FOV.

FRET is a nonradiative process that is sensitive to the distance between two fluorophores (a donor and acceptor (42)) and as such has been termed a "molecular ruler" (43). When employed at the single-molecule level, smFRET can overcome ensemble and time averaging, yielding information on molecular complex formation, conformation, and dynamics (reviewed in (44,45)). Although these applications require the measurement of relative FRET efficiencies, methods for absolute distance measurement have now been established (12,46) and used to determine structural models of dynamic biomolecular complexes (47–50).

To benchmark the smFRET capability of our CoCoS system, we used it to measure precise distances between two dyes in three smFRET standards, according to Hellenkamp et al. (12). The standards were validated in a multilaboratory benchmark study and serve to assess the precision and accuracy of smFRET measurements. These standards are composed of short synthetic DNA molecules labeled with a donor (ATTO 550) and an acceptor (ATTO 647N) separated by 23, 15, and 11 bp, exhibiting low-, mid-, and high-FRET efficiencies, respectively (see Fig. 4 a). The smFRET standards were adsorbed to positively charged cover slips and were imaged using alternating laser excitation (ALEX) (51) with RPA = 174°. At this RPA, each standard appears as a pair of PSFs representing the donor and acceptor emissions. Multiple FOVs were recorded for each of the samples, at a frame rate of 3.3 Hz, alternating between 561 nm (donor excitation) and 638 nm (acceptor excitation). The single molecules' emission signals were then localized, with donor emission dispersed just below the acceptor emission for each labeled DNA molecule (Fig. 4, b and c). Imaging the two emission signals in the same light path eliminates mismatches between channels caused by channel-specific aberrations and optical alignment. It also allows immediate real-time identification of donor-acceptor pairs
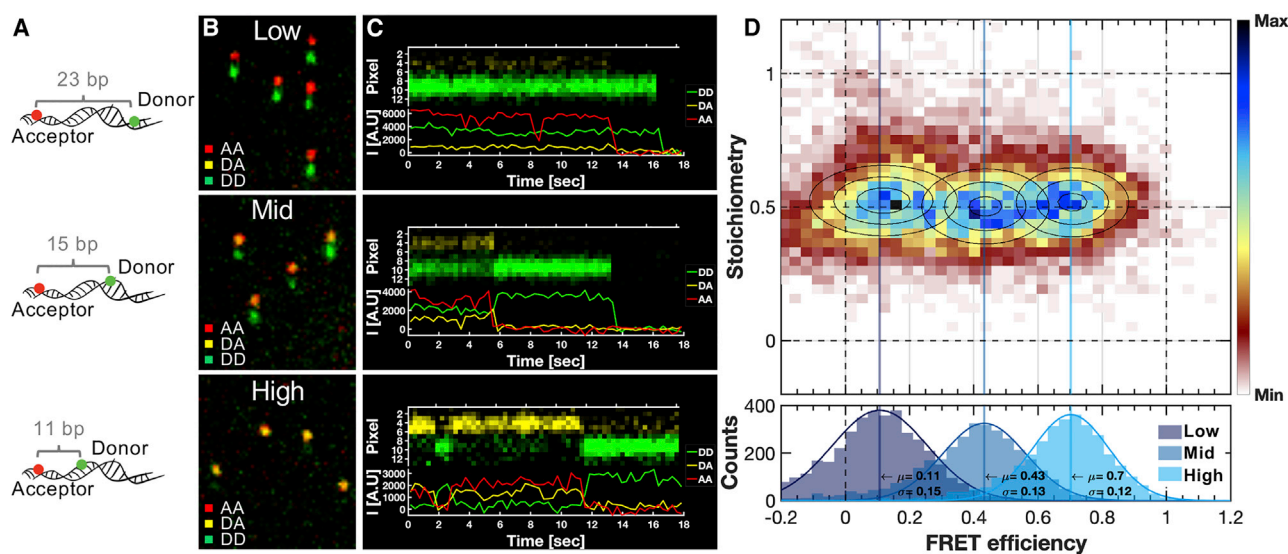

FIGURE 4 Benchmark smFRET analysis with CoCoS. (A) Schematic drawing of the smFRET standard samples used in this experiment. Distances between donor (ATTO 550) and acceptor (ATTO 647N) are stated in base pairs. (B) Representative cropped FOVs of the different standard samples imaged with RPA of 174°. The images show false-colored emission pairs in the FOV with donor excitation at 561 nm (green) and acceptor excitation at 638 nm (red). The acceptor emission is dispersed above the donor emission, in which overlapping signals in the green and red channels represent high acceptor emission with donor excitation (i.e., high FRET appearing yellow). (C) Representative kymographs and intensity time traces. At the top of each panel, a false-colored kymograph of a single smFRET pair emission excited with donor excitation (561 nm). The acceptor's signal (yellow) and the donor's signal (green) are visualized in the CoCoS system one on top of the other, reducing channel registration complexity. Intensity time traces are presented at the bottom of each panel: donor emission with donor excitation (DD, green), acceptor emission with donor excitation (DA, yellow), and acceptor emission with acceptor excitation (AA, red). (D) E-S histogram (10,722 time points recorded from 439 molecules) of the three smFRET samples after applying correction factors and removing donor-only and acceptor-only time points. The fitted FRET efficiency distributions per sample (low: 142 molecules and 4098 time points; mid : 157 molecules and 3390 time points; and high: 140 molecules and 3234 time points) are presented at the bottom panel, with their mean (μ) and SD (σ).
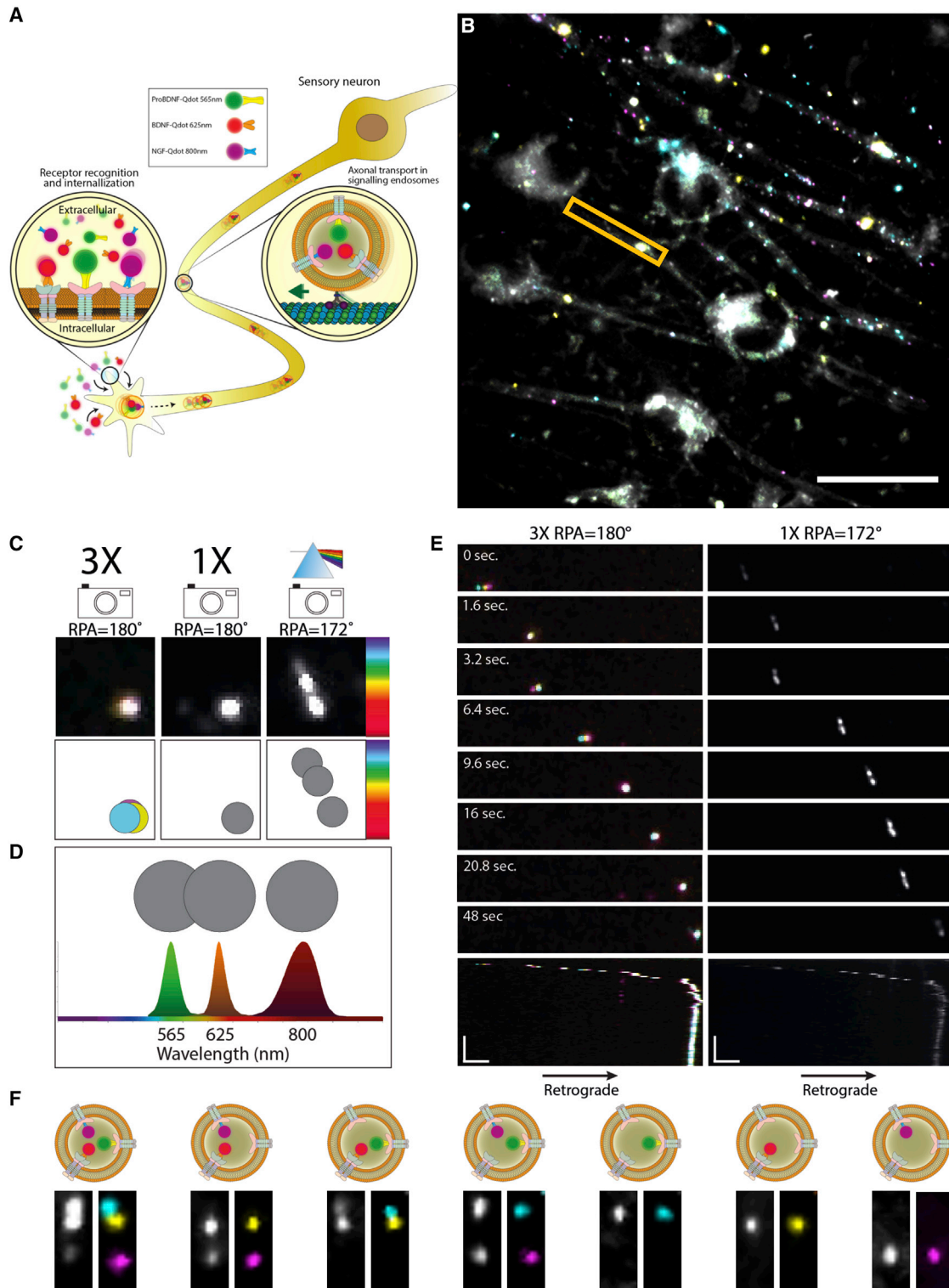
FIGURE 5 Multicolor single-particle tracking of axonal transport in live neurons. (*A*) Schematic illustration describing distal axonal uptake of the different neurotrophic factors and their transportation to the proximal axon and cell body through endosomes. The three neurotrophic factors used in this experiment, proBDNF, BDNF, and NGF, were labeled with Qdot565 (*green*), Qdot625 (*red*), and Qdot800 (*magenta*), respectively. (*B*) False-colored overlay of time-averaged localization (RPA = 180°) full FOV time lapse, processed with background removal. In each frame, four consecutive acquisitions with emission filter switching were taken (*white*, no filter; *cyan*, 575/15; *yellow*, 605/15; and *magenta*, 809/81) and 405 nm excitation. The FOV shows the signaling activity in the proximal axons near neuronal cell bodies. Orange rectangle marks the axon presented in (*E*). Scale bars, 30 μm. (*C*) PSF examples of an endosome transporting all three neurotrophic factors through the axon marked in (*B*). Left: three sequential

without postprocessing, removing the need for split-view emission channel registration. Time traces of donor emission with donor excitation (DD), acceptor emission with donor excitation (DA), and acceptor emission with acceptor excitation (AA) were calculated with local background subtraction (Fig. 4 c). Using the DD, DA, and AA traces, both FRET efficiency (E) and S traces were calculated per molecule and corrected using a standardized procedure (12) (see Fig. 4 c for traces and Supporting materials and methods for full description of the correction procedure and calculated correction factors). The corrected E and S values in each frame before the first bleaching event of either donor or acceptor were then plotted in a 2d histogram to show the different sample distributions (Fig. 4 d, top panel). The ensemble-averaged dye pair FRET distances ($R_{\langle E \rangle}$) were extracted from the sample-specific FRET efficiency distributions, giving $R_{\langle E \rangle}$ = 54.3 ± 3.8, 65.8 ± 4.6, and 88.4 ± 6.2 Å for the high, mid, and low FRET species, respectively. These results stand in good agreement with the average experimental results from the multilab blind study (12) ($R_{\langle E \rangle}$: 51.8 ± 0.7, 60.3 ± 1.3, and 83.4 ± 2.5 Å for the high, mid, and low FRET species, respectively). Our measurements show a slight increase in the calculated distances for all standards. This difference could be caused by the altered surface-attachment procedure applied to the DNA molecules in our experiment, which were not tethered by their ends but rather adsorbed to the surface.

The low dispersion and the lack of dichroic mirrors in the emission path enabled us to maintain a nearly diffraction-limited PSF for each of the colors. Thus, CoCoS provides good SNR and single-molecule sensitivity even with epi-illumination, eliminating the need for the more complex and lower throughput TIRF illumination, which is the standard in the smFRET field. The CoCoS FOV is more than sixfold larger than that of conventional dual-channel TIRF microscopes (50 × 50 μm^2), enabling much higher throughput for smFRET measurements. In this case, only three FOVs per sample had to be analyzed to achieve the presented results. More importantly, because RPA of 174° is sufficient for the spectral separation of all five-color channels in our system, additional FRET pairs could be easily added without any change to the setup or to the dispersion, allowing multicolor smFRET experiments with almost no reduction in throughput or time resolution.

Tracking axonal transport of multiprotein complexes in single endosomes

Most cellular functions are mediated through protein-protein interactions, formation of protein complexes, and their proper spatiotemporal localization, which is largely regulated by trafficking events. Axonal transport is one such process and is essential for neuronal function, survival, differentiation, and maintenance (52). Tracing the retrograde active movement of neurotrophic factors such as NGF, BDNF, and proBDNF within the axon at single-particle resolution had allowed the elucidation of key mechanisms of neuronal signaling (53–55). However, as single-molecule transport studies mainly focus on characterizing the transport of a single protein type per experiment, an open question in the field is whether multiprotein complexes transport together within a single endosome (56).

To characterize axonal transport, we cultured embryonic DRG in microfluidic chambers that enable the directional growth of axons into an isolated compartment (35,57). Once axons have extensively crossed into this compartment, we applied a mixture of proteins NGF, BDNF, and proBDNF labeled with Qdot-800, Qdot-625, and Qdot-565, respectively, exclusively to the compartment containing the distal axon as illustrated in Fig. 5 a. The uptake and axonal transport of these three neurotrophic factors into the same axons was recorded by time-lapse imaging in CoCoS color-detection mode with the minimal dispersion required to resolve the three markers (RPA = 172°), followed by the standard consecutive color acquisition by emission filter switching in CoCoS localization mode (RPA = 180°) (see Materials and methods). Fig. 5 b presents a time-averaged FOV showing the signaling activity in the proximal axons near the neuronal cell bodies.

Working in CoCoS color-detection mode allowed us to visualize the labeled proteins inside individual endosomes in a single acquisition (Fig. 5, c and d), completely avoiding the spatiotemporal inaccuracies

localization (RPA = 180°) acquisitions with emission filters switching (same color code as in (B)). Middle: single localization (RPA = 180°) acquisition with no emission filter. Right: CoCoS color-detection mode with no emission filter and optimal dispersion (RPA = 172°); color bar on the right illustrates the spectral-dispersion map (nonaccurate). (D) Theoretical spectra of the three Qdots with PSF visual representation for illustration purposes (nonaccurate. For a theoretically calculated dispersed PSF, see Fig. S13). (E) Example time-lapse frames followed by a kymograph of the marked axon in (B), showing the retrograde transport of the endosome presented in (C). Left: three consecutive acquisitions per frame are shown with RPA = 180°, 405 nm excitation, and 575/15 (cyan), 605/15 (yellow), and 809/81 (magenta) emission filters. A spatiotemporal mismatch between the acquisitions is clearly visible when the transport velocity is high (0, 3.2, and 6.4 s frames). Right: a single acquisition per frame is shown with no emission filter and with RPA = 172°. At the bottom of each time lapse, a kymograph of the full time lapse is presented, showing a halt in transportation at cell death after 30 s of imaging. Horizontal scale bars, 3 μm; vertical scale bars, 30 s. (F) Example of CoCoS PSFs for each of the protein combinations inside the transporting endosomes as detected in the FOV of (B). Left: single acquisition with RPA = 172°. Right: false-color overlay of three consecutive acquisitions with RPA = 172° and emission filters switching.

inherent to multicolor single-molecule tracking using consecutive color acquisition (comparison shown in Fig. 5 e). Furthermore, the photophysical properties of Qdots, which have broad excitation spectra and a narrow emission peak (see Fig. 5 d for the theoretical spectra of the Qdots used in this experiment and Fig. S13 for the theoretical CoCoS spectral PSF calculation), coupled with CoCoS simultaneous multicolor detection, allowed us to track all markers with a single laser excitation per frame (as opposed to three in consecutive imaging), enabling up to a threefold increase in acquisition rate, coupled with a significantly (66%) reduced cellular photodamage.

As above (far-red dye classification section), two consecutive frames with different RPAs (localization, RPA = 180°, followed by color detection, RPA = 172°) were used to spectrally classify single markers transported in the endosome. With 80 ms switching time between the RPAs, the time cost of this acquisition mode is comparable to a single filter wheel switch but enables the resolution of multiple colors with only two frames. When two or more markers are transported in the same endosome, the full protein content can be inferred in a single frame from the relative displacement of the different color markers. These relative displacements create a unique spectral signature for multimarker combinations (as illustrated by the examples of endosomal protein combinations in Fig. 5 f), eliminating the need for an additional calibration frame. Future experimental designs could exploit this feature, for example by labeling the endosome membrane with an additional color to provide a spectral reference for each endosome, allowing the spectral identification of individual markers in a single frame, thus further increasing the time resolution and reducing phototoxicity.

Our results from tracking the retrograde transportation of multiple neurotrophins showed a non-negligible portion of the endosomes transporting two or three types of neurotrophins together within the same endosome (Fig. 5, d and f). This is an intriguing observation as previous single-molecule tracking of NGF transportation found that the majority of NGF containing endosomes contained only a single NGF dimer (54).

DISCUSSION

CoCoS microscopy is an optical add-on to wide-field epi-fluorescence microscopy, which allows continuous control over the spectral resolution of the system. A key feature of CoCoS is the ability to easily switch between different modes of operation: 1) imaging and localization, 2) color detection/FRET, and 3) spectral analysis. With our epi-fluorescence microscope system, we showed the ability to detect and localize up to five color channels simultaneously, affording up to

a fivefold reduction in multichannel acquisition time and significantly enhancing throughput in multicolor experiments. The flexibility in setting the spectral resolution and maximizing both SNR and throughput in CoCoS had enabled us to perform a diverse range of applications: spectral classification of three red dyes excited by a single laser, smFRET under epi-illumination, and multicolor tracking in a highly complex and noisy biological environment. These represent popular applications that are easily enhanced or simplified by CoCoS microscopy. Moreover, the number of detectable color channels is only limited by the fluorophores' spectra and the transmission bands of the MM and band-pass filter used in the experiment. Thus, future work can easily expand the number of possible emission channels in the color-detection mode.

The key limitation of our current system stems from the prisms used in this setup. These are currently low-cost, off-the-shelf prisms, which have a small cross section that introduced optical aberrations at small RPAs because of the large field of illumination. Furthermore, the nonlinear dispersion of the prisms created varying spectral resolution across the spectrum, forcing different RPA for the same spectral resolution in different wavelengths. This will be improved in future work by carefully designing the prism material and apex angles (58). Another limitation for spectral analysis with the current CoCoS system arises in cases in which only a single-color channel is detected per PSF. These cases require two consecutive frames to localize the fluorescent markers (in the first frame) and to read out the spectral information (in the second frame). This limitation does not apply when two or more colors are detected because each color combination creates a distinct PSF and does not require a spatial reference. Thus, it would not affect smFRET experiments in which two or more channels are used and could be easily resolved in tracking experiments by reference labeling all tracked species with the same color. In cases of single-color-channel spectroscopy, this limitation could be addressed in future versions of CoCoS by 1) improving the rotation velocity of the motorized prism rotators to achieve minimal rotation time (<10 ms between localization to sub-nm/pixel spectral resolution with commercial rotators) and performing fast alternating laser excitation-like alternating localization-spectral imaging; 2) introducing dual-camera or split-view configuration in which CoCoS is positioned in the spectral path as performed in current spectral imaging systems; and 3) introducing single acquisition marker detection based on machine-learning PSF classification, as will be discussed in the following paragraph.

Future solutions may involve deep learning-based deconvolution because the detection of color in CoCoS is based on the spatial intensity distribution of spectral

PSFs. Recent incorporation of deep learning for PSF analysis (59) has shown that small variations in PSF could be exploited for color detection and differentiation between markers. With CoCoS, minute and well-calibrated color-dependent PSF changes can be easily introduced, allowing full-color PSF detection by deep learning. Unlike PSF-based color detection in which a liquid-crystal spatial light modulator device is used to control the PSF (59), CoCoS has almost no photon loss, making it much more suitable for low SNR settings typical for single molecules in biological contexts.

The ability to record multiple emission color channels simultaneously with optimized SNR and throughput and without splitting the FOV opens the door for highly multiplexed smFRET experiments. Utilizing multiple donor-acceptor pairs will allow better reconstruction of molecular structure and dynamics for proteins or other molecular assemblies (60). This feature not only expands the current limit on multicolor smFRET, which currently stands on four colors (6,44), but also dramatically simplifies the optical setup while expanding the FOV and throughput of the system by more than fivefold. With the current ability to quickly toggle between localization and full spectral information, both tracking and differentiating multiple single-molecule markers within the same spectral window is made possible. This makes CoCoS attractive for multicomponent single-molecule tracking with full spectral information. Furthermore, the available spectral recording may be utilized to measure environmental- (10,40) or voltage- (41) dependent single-molecule spectral shifts with optimized spectral resolution.

SUPPORTING MATERIAL

Supporting material can be found online at https://doi.org/10.1016/j.bpr.2021.100013.

REFERENCES

1. Ha, T. 2014. Single-molecule methods leap ahead. *Nat. Methods.* 11:1015–1018.

2. Joo, C., H. Balci, …, T. Ha. 2008. Advances in single-molecule fluorescence methods for molecular biology. *Annu. Rev. Biochem.* 77:51–76.

3. Sako, Y., and T. Yanagida. 2003. Single-molecule visualization in cell biology. *Nat. Rev. Mol. Cell Biol.* Suppl:SS1–SS5.

4. Garini, Y., I. T. Young, and G. McNamara. 2006. Spectral imaging: principles and applications. *Cytometry A.* 69:735–747.

5. Douglass, K. M., C. Sieben, …, S. Manley. 2016. Super-resolution imaging of multiple cells by optimised flat-field epi-illumination. *Nat. Photonics.* 10:705–708.

6. Lee, J., S. Lee, …, S. Hohng. 2010. Single-molecule four-color FRET. *Angew. Chem. Int. Ed. Engl.* 49:9922–9925.

7. Dong, B., L. Almassalha, …, H. F. Zhang. 2016. Super-resolution spectroscopic microscopy via photon localization. *Nat. Commun.* 7:12290.

8. Zhang, Z., S. J. Kenny, …, K. Xu. 2015. Ultrahigh-throughput single-molecule spectroscopy and spectrally resolved super-resolution microscopy. *Nat. Methods.* 12:935–938.

9. Mlodzianoski, M. J., N. M. Curthoys, …, S. T. Hess. 2016. Super-resolution imaging of molecular emission spectra and single molecule spectral fluctuations. *PLoS One.* 11:e0147506.

10. Bongiovanni, M. N., J. Godet, …, S. F. Lee. 2016. Multi-dimensional super-resolution imaging enables surface hydrophobicity mapping. *Nat. Commun.* 7:13544.

11. Huang, T., C. Phelps, …, X. Nan. 2018. Simultaneous multicolor single-molecule tracking with single-laser excitation via spectral imaging. *Biophys. J.* 114:301–310.

12. Hellenkamp, B., S. Schmid, …, T. Hugel. 2018. Precision and accuracy of single-molecule FRET measurements-a multi-laboratory benchmark study. *Nat. Methods.* 15:669–676.

13. Suzuki, Y., T. Tani, …, S. Kamimura. 2002. Imaging of the fluorescence spectrum of a single fluorescent molecule by prism-based spectroscopy. *FEBS Lett.* 512:235–239.

14. Haga, T., T. Sonehara, …, S. Takahashi. 2013. Prism-based spectral imaging of four species of single-molecule fluorophores by using one excitation laser. *J. Fluoresc.* 23:591–597.

15. Lundquist, P. M., C. F. Zhong, …, D. Zaccarin. 2008. Parallel confocal detection of single molecules in real time. *Opt. Lett.* 33:1026–1028.

16. Eid, J., A. Fehr, …, S. Turner. 2009. Real-time DNA sequencing from single polymerase molecules. *Science.* 323:133–138.

17. Song, K.-H., Y. Zhang, …, H. F. Zhang. 2020. Symmetrically dispersed spectroscopic single-molecule localization microscopy. *Light Sci. Appl.* 9:92.

18. Zhang, Y., K.-H Song, …, H. F. Zhang. 2019. Multicolor super-resolution imaging using spectroscopic single-molecule localization microscopy with optimal spectral dispersion. *Appl. Opt.* 58:2248–2255.

19. Yan, R., S. Moon, …, K. Xu. 2018. Spectrally resolved and functional super-resolution microscopy via ultrahigh-throughput single-molecule spectroscopy. *Acc. Chem. Res.* 51:697–705.

20. Sansalone, L., Y. Zhang, …, F. M. Raymo. 2019. High-throughput single-molecule spectroscopy resolves the conformational isomers of BODIPY chromophores. *J. Phys. Chem. Lett.* 10:6807–6812.

21. Lee, J. E., J. C. Sang, …, D. Klenerman. 2018. Mapping surface hydrophobicity of α-synuclein oligomers at the nanoscale. *Nano Lett.* 18:7494–7501.

22. Moon, S., R. Yan, …, K. Xu. 2017. Spectrally resolved, functional super-resolution microscopy reveals nanoscale compositional heterogeneity in live-cell membranes. *J. Am. Chem. Soc.* 139:10944–10947.

23. Stern, H. L., R. Wang, …, S. F. Lee. 2019. Spectrally resolved photodynamics of individual emitters in large-area monolayers of hexagonal boron nitride. *ACS Nano.* 13:4538–4547.

24. Brenner, B., K.-H. Song, …, H. F. Zhang. 2021. Improving spatial precision and field-of-view in wavelength-tagged single-particle tracking using spectroscopic single-molecule localization microscopy. *Appl. Opt.* 60:3647–3658.

25. Song, K.-H., B. Dong, …, H. F. Zhang. 2018. Theoretical analysis of spectral precision in spectroscopic single-molecule localization microscopy. *Rev. Sci. Instrum.* 89:123703.

26. Dong, B., J. L. Davis, …, H. F. Zhang. 2018. Spectroscopic analysis beyond the diffraction limit. *Int. J. Biochem. Cell Biol.* 101:113–117.

27. Kim, D., Z. Zhang, and K. Xu. 2017. Spectrally resolved super-resolution microscopy unveils multipath reaction pathways of single spiropyran molecules. *J. Am. Chem. Soc.* 139:9447–9450.

28. Liu, X., L. Yao, …, J. Ma. 2019. Spectroscopic fluorescent tracking of a single molecule in a live cell with a dual-objective fluorescent reflection microscope. *Appl. Phys. Express.* 12:112007.

29. Wynne, C. G. 1997. Atmospheric dispersion in very large telescopes with adaptive optics. *Mon. Not. R. Astron. Soc.* 285:130–134.

30. Donati, G. B., N. O. A. Str, and D. S. Stellari. 1862. Intorno alle strie degli spettri stellari. *Nuovo Cim.* 15:292–304.

31. Wynne, C. G., and S. P. Worswick. 1986. Atmospheric dispersion correctors at the Cassegrain focus. *Mon. Not. R. Astron. Soc.* 220:657–670.

32. Edelstein, A., N. Amodaj, …, N. Stuurman. 2010. Computer control of microscopes using μManager. *Curr. Protoc. Mol. Biol.* Chapter 14:Unit14.20.

33. Edelstein, A. D., M. A. Tsuchida, …, N. Stuurman. 2014. Advanced methods of microscope control using μManager software. *J. Biol. Methods.* 1:10.

34. Torchinsky, D., and Y. Ebenstein. 2016. Sizing femtogram amounts of dsDNA by single-molecule counting. *Nucleic Acids Res.* 44:e17.

35. Gluska, S., M. Chein, …, E. Perlson. 2016. Tracking Quantum-Dot labeled neurotropic factors transport along primary neuronal axons in compartmental microfluidic chambers. *Methods Cell Biol.* 131:365–387.

36. Natan, A. 2013. Fast 2D peak finder, MATLAB Central File Exchange. Retrieved October 2, 2020 https://www.mathworks.com/matlabcentral/fileexchange/37388-fast-2d-peak-finder.

37. Schindelin, J., I. Arganda-Carreras, …, A. Cardona. 2012. Fiji: an open-source platform for biological-image analysis. *Nat. Methods.* 9:676–682.

38. Preus, S., S. L. Noer, …, V. Birkedal. 2015. iSMS: single-molecule FRET microscopy software. *Nat. Methods.* 12:593–594.

39. Moon, S. L., T. Morisaki, …, T. J. Stasevich. 2019. Multicolour single-molecule tracking of mRNA interactions with RNP granules. *Nat. Cell Biol.* 21:162–168.

40. Klymchenko, A. S. 2017. Solvatochromic and fluorogenic dyes as environment-sensitive probes: design and biological applications. *Acc. Chem. Res.* 50:366–375.

41. Kuo, Y., J. Li, …, S. Weiss. 2018. Characterizing the quantum-confined Stark effect in semiconductor quantum dots and nanorods for single-molecule electrophysiology. *ACS Photonics.* 5:4788–4800.

42. Förster, T. 1948. Zwischenmolekulare Energiewanderung und Fluoreszenz. *Ann. Phys.* 437:55–75.

43. Stryer, L., and R. P. Haugland. 1967. Energy transfer: a spectroscopic ruler. *Proc. Natl. Acad. Sci. USA.* 58:719–726.

44. Lerner, E., A. Barth, …, S. Weiss. 2021. FRET-based dynamic structural biology: challenges, perspectives and an appeal for open-science practices. *Elife.* 10:e60416.

45. Hohlbein, J., T. D. Craggs, and T. Cordes. 2014. Alternating-laser excitation: single-molecule FRET and beyond. *Chem. Soc. Rev.* 43:1156–1171.

46. Lee, N. K., A. N. Kapanidis, …, S. Weiss. 2005. Accurate FRET measurements within single diffusing biomolecules using alternating-laser excitation. *Biophys. J.* 88:2939–2953.

47. Kalinin, S., T. Peulen, …, C. A. M. Seidel. 2012. A toolkit and benchmark study for FRET-restrained high-precision structural modeling. *Nat. Methods.* 9:1218–1225.

48. Hellenkamp, B., P. Wortmann, …, T. Hugel. 2017. Multidomain structure and correlated dynamics determined by self-consistent FRET networks. *Nat. Methods.* 14:174–180.

49. Craggs, T. D., M. Sustarsic, …, A. N. Kapanidis. 2019. Substrate conformational dynamics facilitate structure-specific recognition of gapped DNA by DNA polymerase. *Nucleic Acids Res.* 47:10788–10800.

50. Nagy, J., D. Grohmann, …, J. Michaelis. 2015. Complete architecture of the archaeal RNA polymerase open complex from single-molecule FRET and NPS. *Nat. Commun.* 6:6161.

51. Kapanidis, A. N., N. K. Lee, …, S. Weiss. 2004. Fluorescence-aided molecule sorting: analysis of structure and interactions by alternating-laser excitation of single molecules. *Proc. Natl. Acad. Sci. USA.* 101:8936–8941.

52. Zahavi, E. E., R. Maimon, and E. Perlson. 2017. Spatial-specific functions in retrograde neuronal signalling. *Traffic.* 18:415–424.

53. Zhang, K., Y. Osakada, …, B. Cui. 2010. Single-molecule imaging of NGF axonal transport in microfluidic devices. *Lab Chip.* 10:2566–2573.

54. Cui, B., C. Wu, …, S. Chu. 2007. One at a time, live tracking of NGF axonal transport using quantum dots. *Proc. Natl. Acad. Sci. USA.* 104:13666–13671.

55. Zhao, X., Y. Zhou, …, C. Wu. 2014. Real-time imaging of axonal transport of quantum dot-labeled BDNF in primary neurons. *J. Vis. Exp* 51899.

56. Terenzio, M., G. Schiavo, and M. Fainzilber. 2017. Compartmentalized signaling in neurons: from cell biology to neuroscience. *Neuron.* 96:667–679.

57. Ionescu, A., T. Gradus, …, E. Perlson. 2019. Targeting the sigma-1 receptor via pridopidine ameliorates central features of ALS pathology in a SOD1^{G93A} model. *Cell Death Dis.* 10:210.

58. Hagen, N., and T. S. Tkaczyk. 2011. Compound prism design principles, II: triplet and Janssen prisms. *Appl. Opt.* 50:5012–5022.

59. Hershko, E., L. E. Weiss, …, Y. Shechtman. 2019. Multicolor localization microscopy and point-spread-function engineering by deep learning. *Opt. Express.* 27:6158–6183.

60. Wei, X., J. Nangreave, …, Y. Liu. 2013. Mapping the thermal behavior of DNA origami nanostructures. *J. Am. Chem. Soc.* 135:6165–6176.